ESAIM: Proceedings, Vol. 1, 1996, pp. 463–479
http://www.emath.fr/proc/Vol.1/

Singularity Formation in the Shape of a Vortex Sheet in Three Dimensions—Numerical Simulation

Takashi Ishihara
Department of Mathematics
Faculty of Science
Toyama University
Gofuku, Toyama 930, Japan

Yukio Kaneda
Department of Applied Physics
Faculty of Engineering
Nagoya University
Chikusa-ku, Nagoya 464-01, Japan

Abstract

The evolution of a small but finite three-dimensional disturbance on a flat uniform vortex sheet is studied numerically on the basis of a Lagrangian representation of the motion. The numerical simulations confirm the asymptotic analysis by Ishihara and Kaneda (1995; *J. Fluid Mech.*, **300**, 339-366) for the spontaneous singularity formation in the shape of the vortex sheet. They also suggest that the singularities appear along curves, which have a rather simple dependence on the spanwise-coordinate. Reflecting the three-dimensionality of the vortex dynamics, the singularity-curve is not along any of the vortex lines.

1 Introduction

Dynamics of vortex sheets in three-dimensional flow is fundamentally different from that in two-dimensional one, particularly because of the existence of vortex stretching mechanism in three dimensions. In spite of the fact that most real flows are three-dimensional, little is known about three-dimensional motion of vortex sheets, as compared with two-dimensional motion.

Regarding two-dimensional motion of a vortex sheet, Moore [6] studied analytically the evolution of a small but finite streamwise disturbance on a flat uniform vortex sheet by using Birkhoff-Rott equation, and gave an analytical evidence for the spontaneous singularity formation in the shape of the vortex sheet. His analysis gives a fairly good prediction of the appearance time as well as the form and location of a singularity even for the case of finite disturbance investigated numerically by Meiron et al. [7], Krasny [5] and Shelley [8].

Recently, Ishihara and Kaneda [3] (hereinafter referred to as IK) studied the evolution of a small but finite three-dimensional disturbance on a flat uniform vortex sheet by generalizing Moore's analysis to three dimensions on the basis of a Lagrangian representation of the three-dimensional motion of a vortex sheet (Caflisch [2], Kaneda [4]). In IK, the vortex sheet at time t is expanded in a double periodic Fourier series:

$$\mathbf{R}(\lambda_1, \lambda_2, t) = (\lambda_1, \lambda_2, 0) + \sum_{n,m} \mathbf{A}_{n,m} \exp[\mathrm{i}(n\lambda_1 + \delta m \lambda_2)], \tag{1}$$

where λ_1 and λ_2 are Lagrangian parameters in the streamwise and spanwise directions, respectively, and δ is the aspect ratio of the periodic domain of the disturbance. An asymptotic analysis valid at large t showed that a singularity appears at a finite time $t_c = O(\ln \epsilon^{-1})$ where ϵ is the the amplitude of the initial disturbance. The singularity is such that $\mathbf{A}_{n,0} = O(t_c^{-1})$ behaves like $n^{-5/2}$, while

$\mathbf{A}_{n,\pm1} = O(\epsilon t_c)$ behaves like $n^{-3/2}$ for large n. The former agrees with the two-dimensional result in Moore [6], while the latter reflects three-dimensionality or vortex stretching.

The full determination of the location as well as the form and the appearance time of the singularity would require the full asymptotics of $\mathbf{A}_{n,m}$ for large n and m. However, being based on the treatment of a rather limited range of (n, m), the analysis of IK is insufficient for the full determination. The purpose of this paper is to study *numerically* the three-dimensional motion of a vortex sheet so as to get further understanding of the singularity formation process of a vortex sheet in three dimensions. Particular attention is paid to the meaning of the three-dimensional correction term $\mathbf{A}_{n,\pm1}$.

The problem definition and a short review of IK for the weak nonlinear problem are given in Section 2, where some possible interpretations of the term $\mathbf{A}_{n,\pm1}$ are also presented. Section 3 presents a numerical method based on the Lagrangian representation of the three-dimensional motion of a vortex sheet. Section 4 presents the numerical results. They confirm the analytical results in IK, and we check the above interpretations in the light of the numerical results. Conclusions and discussion are presented in Section 5.

2 Problem definition and analytical results for the weak nonlinear case

Let a vortex sheet be described parametrically by $\mathbf{R}(\lambda_1, \lambda_2, t)$, and let us consider a flat uniform vortex sheet. Suppose that it is perturbed initially as

$$\mathbf{R}(\lambda_1, \lambda_2, 0) = (\lambda_1, \lambda_2, 0) + (\epsilon_2 \sin 2\pi\delta\lambda_2, 0, \epsilon_1 \sin 2\pi\lambda_1), \tag{2}$$

where λ_1 and λ_2 are the Lagrangian parameters in the streamwise and spanwise directions, respectively. Then the motion is given by

$$\frac{\partial}{\partial t}\mathbf{R} = \text{p.v.} \int_{-\infty}^{\infty}\int_{-\infty}^{\infty} (\nabla G) \times \frac{\partial \mathbf{R}'}{\partial \lambda_2'} \mathrm{d}\lambda_1' \mathrm{d}\lambda_2', \;\; G \equiv \frac{1}{4\pi}\frac{1}{|\mathbf{R} - \mathbf{R}'|}, \tag{3}$$

where the symbol p.v. denotes the principal value of the integral, $\mathbf{R} \equiv \mathbf{R}(\lambda_1, \lambda_2, t)$, $\mathbf{R}' \equiv \mathbf{R}(\lambda_1', \lambda_2', t)$ and $\nabla \equiv (\partial/\partial\mathbf{R})$ (Caflisch [2], Kaneda [4]). The flow is two-dimensional if $\epsilon_2 = 0$, as assumed by Moore [6]. If $\epsilon_1 = 0$, the vortex sheet is flat but each vortex line is distorted sinusoidally on the flat vortex sheet. Note that we have so parametrized the sheet that $\lambda_1 =$ constant defines a vortex line.

Since the present numerical study on the three-dimensional motion of a vortex sheet is closely related to the analytical study in IK, we briefly review here IK. In the following, we assume appropriate normalization of the time and length scale. The position vector $\mathbf{R}$ at time t may be then expanded in a double periodic Fourier series as

$$\mathbf{R}(\lambda_1, \lambda_2, t) = (\lambda_1, \lambda_2, 0) + \sum_{n,m} \mathbf{A}_{n,m}(t) \exp\{2\pi\mathrm{i}(n\lambda_1 + \delta m \lambda_2)\}. \tag{4}$$

By assuming $\epsilon = \max(\epsilon_1, \epsilon_2)$ to be small but finite and by introducing the following ordering as in Moore [6]:

$$\begin{aligned} \mathbf{A}_{n,m} \;=\; & (2\pi\epsilon_1)^{|n|}(2\pi\epsilon_2)^{|m|}\mathbf{A}_{n,m}^{(0)} + (2\pi\epsilon_1)^{|n|+2}(2\pi\epsilon_2)^{|m|}\mathbf{A}_{n,m}^{(2,0)} + \cdots \\ & + (2\pi\epsilon_1)^{|n|}(2\pi\epsilon_2)^{|m|+2}\mathbf{A}_{n,m}^{(0,2)} + \cdots, \end{aligned} \tag{5}$$

IK obtained a closed set of equations for $\{\mathbf{A}^{(0)}_{n,m}\}$. The solution of the set for large t was found inductively to be expressed as

$$\mathbf{A}^{(0)}_{n,\pm m} = \mathrm{i}\left(\mp\frac{\delta}{4}\right)^m \left(-\frac{1}{4}\right)^n \mathrm{e}^{\pi n t}\left[\mathbf{a}^{(0)}_{n,\pm m}(2\pi t)^{n-1+2m} + \mathbf{a}^{(1)}_{n,\pm m}(2\pi t)^{n-2+2m} + \ldots\right] + O(\mathrm{e}^{\pi(n-1)t}), \quad (6)$$

for $n > 0$ and $m \geq 0$. Note that (5) and (6) give

$$|\mathbf{A}_{n,\pm(m+1)}|/|\mathbf{A}_{n,\pm m}| = O(\epsilon_2 t^2), \quad (7)$$

for large t and small ϵ. Since the time t under consideration is $O(\ln \epsilon_1^{-1})$, (7) implies that when ϵ_2 is small enough, the Fourier coefficients for small m are important.

The coefficients $\mathbf{a}^{(0)}_{n,0} = (a^{(0)}_{n,0}, b^{(0)}_{n,0}, c^{(0)}_{n,0})$ and $\mathbf{a}^{(0)}_{n,\pm 1} = (a^{(0)}_{n,\pm 1}, b^{(0)}_{n,\pm 1}, c^{(0)}_{n,\pm 1})$ in (6) can be obtained from the following relations:

$$a^{(0)}_{n,0} = c^{(0)}_{n,0} = \frac{1}{2(n-1)}\sum_{k=1}^{n-1} k(n-k)c^{(0)}_{k,0}c^{(0)}_{n-k,0}, \quad b^{(0)}_{n,0} = 0, \quad (8)$$

with $a^{(0)}_{1,0} = c^{(0)}_{1,0} = 1$ and $b^{(0)}_{1,0} = 0$, and

$$\begin{aligned} 2n(n+1)c^{(0)}_{n,\pm 1} &= \sum_{k=1}^{n}\left\{ n^2 k - (n^2 - nk + k^2)(n^2+\delta^2)^{\frac{1}{2}} + \frac{k(n-k)^2(n^2+\delta^2)^{\frac{1}{2}}}{[(n-k)^2+\delta^2]^{\frac{1}{2}}}\right. \\ &\left. + \frac{n(n-k)(n^2 - nk + \delta^2)}{[(n-k)^2+\delta^2]^{\frac{1}{2}}}\right\} c^{(0)}_{n-k,\pm 1}a^{(0)}_{k,0}, \quad (9a) \end{aligned}$$

$$a^{(0)}_{n,\pm 1} = \frac{n}{(n^2+\delta^2)^{\frac{1}{2}}}c^{(0)}_{n,\pm 1}, \quad (9b)$$

$$b^{(0)}_{n,\pm 1} = \frac{\pm\delta}{(n^2+\delta^2)^{\frac{1}{2}}}c^{(0)}_{n,\pm 1}, \quad (9c)$$

with $a^{(0)}_{0,\pm 1} = b^{(0)}_{0,\pm 1} = 0$ and $c^{(0)}_{0,\pm 1} = 1$, where the sum $\sum_{k=1}^{n}$ is zero when $n < 1$. It is shown numerically that $a^{(0)}_{n,0}, c^{(0)}_{n,0}$ and $b^{(0)}_{n,\pm 1}$ behave like $\mathrm{e}^n n^{-5/2}$, while $a^{(0)}_{n,\pm 1}$ and $c^{(0)}_{n,\pm 1}$ behave like $\mathrm{e}^n n^{-3/2}$ for large n independently of δ. It is shown analytically that $a^{(0)}_{n,\pm 1} = c^{(0)}_{n,\pm 1} \propto \mathrm{e}^n n^{-3/2}$ for $\delta \ll 1$. The leading-order asymptotic forms of $\mathbf{A}_{n,0} = (X_{n,0}, Y_{n,0}, Z_{n,0})$ and $\mathbf{A}_{n,\pm 1} = (X_{n,\pm 1}, Y_{n,\pm 1}, Z_{n,\pm 1})$ for large n and large t are given by

$$X_{n,0} = Z_{n,0} = \mathrm{i}(2\pi)^{-\frac{3}{2}}(-1)^n t_{\mathrm{c}}^{-1} n^{-\frac{5}{2}}(\epsilon_1\theta)^n, \quad (10)$$

$$X_{n,\pm 1} = Z_{n,\pm 1} = \mp\mathrm{i}\pi^2(-1)^n C_\delta \delta(\epsilon_2 t_{\mathrm{c}}) n^{-\frac{3}{2}}(\epsilon_1\theta)^n, \quad (11)$$

and

$$Y_{n,\pm 1} = -\mathrm{i}\pi^2(-1)^n C_\delta \delta^2(\epsilon_2 t_{\mathrm{c}}) n^{-\frac{5}{2}}(\epsilon_1\theta)^n, \quad (12)$$

where $\theta \equiv \theta(t) \equiv \pi^2 \exp(\pi t + 1)$ with the singularity time t_c being determined by $\epsilon_1\theta(t_c) = 1$, and C_δ is a constant depending only on the aspect ratio δ.

Substitution of (5) and (6) into (4) yields an expression of the sheet profile near the singularity time under appropriate conditions (see IK for details);

$$\begin{aligned} x(\lambda_1,\lambda_2,t) &\approx \lambda_1 - \frac{1}{2\pi^2 t}\sum_{n=1}^{\infty}(\epsilon_1\theta)^n \bar{a}^{(0)}_{n,0}\sin 2\pi n(\lambda_1+\tfrac{1}{2}) \\ &\quad +2\pi\delta\epsilon_2 t\Big\{\sum_{n=0}^{\infty}(\epsilon_1\theta)^n \bar{a}^{(0)}_{n,1}\cos 2\pi n(\lambda_1+\tfrac{1}{2})\Big\}\sin 2\pi\delta\lambda_2, \qquad (13a) \\ y(\lambda_1,\lambda_2,t) &\approx \lambda_2 + 2\pi\delta\epsilon_2 t\Big\{\sum_{n=1}^{\infty}(\epsilon_1\theta)^n \bar{b}^{(0)}_{n,1}\sin 2\pi n(\lambda_1+\tfrac{1}{2})\Big\}\cos 2\pi\delta\lambda_2, \qquad (13b) \\ z(\lambda_1,\lambda_2,t) &\approx -\frac{1}{2\pi^2 t}\sum_{n=1}^{\infty}(\epsilon_1\theta)^n \bar{a}^{(0)}_{n,0}\sin 2\pi n(\lambda_1+\tfrac{1}{2}) \\ &\quad +2\pi\delta\epsilon_2 t\Big\{\sum_{n=0}^{\infty}(\epsilon_1\theta)^n \bar{c}^{(0)}_{n,1}\cos 2\pi n(\lambda_1+\tfrac{1}{2})\Big\}\sin 2\pi\delta\lambda_2, \qquad (13c) \end{aligned}$$

where $\bar{a}^{(0)}_{n,0} \equiv a^{(0)}_{n,0}\mathrm{e}^{-n}$, $\bar{a}^{(0)}_{n,\pm1} \equiv a^{(0)}_{n,\pm1}\mathrm{e}^{-n}$, and so on. In deriving (13a–c), we have used the relations $\bar{a}^{(0)}_{n,0} = \bar{c}^{(0)}_{n,0}$, $\bar{a}^{(0)}_{n,1} = \bar{a}^{(0)}_{n,-1}$, $\bar{b}^{(0)}_{n,1} = -\bar{b}^{(0)}_{n,-1}$ and $\bar{c}^{(0)}_{n,1} = \bar{c}^{(0)}_{n,-1}$. Note that putting $\epsilon_2 = 0$ in (13a–c) gives the two-dimensional sheet profile, which is the same as obtained in Moore [6]. The terms proportional to $\epsilon_2 t$ therefore imply three-dimensional correction of the profile near the singularity time.

Note that for two-dimensional motion in which $\epsilon_2 = 0$, the sheet profile near the singularity time is given by

$$\begin{aligned} x(\lambda_1,\lambda_2,t) &\approx \lambda_1 - \frac{1}{2\pi^2 t}\sum_{n=1}^{\infty}(\epsilon_1\theta)^n \bar{a}^{(0)}_{n,0}\sin 2\pi n(\lambda_1+\tfrac{1}{2}), \qquad (14a) \\ y(\lambda_1,\lambda_2,t) &= \lambda_2, \qquad (14b) \\ z(\lambda_1,\lambda_2,t) &\approx -\frac{1}{2\pi^2 t}\sum_{n=1}^{\infty}(\epsilon_1\theta)^n \bar{a}^{(0)}_{n,0}\sin 2\pi n(\lambda_1+\tfrac{1}{2}). \qquad (14c) \end{aligned}$$

Comparison of (13a–c) with (14a–c) suggests us to assume that the three-dimensional sheet profile (13a–c) results from a certain modification of (i) the amplitude $\bar{a}^{(0)}_{n,0}$, (ii) the phase λ_1 and/or (iii) the critical time t_c of the two-dimensional profile due to the three-dimensionality. Among several possible interpretations of (13a–c) based on such an assumption, the simplest is to interpret (13a–c) to result from the modification of only one of (i), (ii) and (iii). Then we are left to the following three interpretations (a), (b) and (c).

Interpretation (a)

If we assume that the three-dimensional correction terms come from the modification of only $\bar{a}^{(0)}_{n,0}$ in the two-dimensional profile, then it may be concluded that a singularity appears at a time t_c defined by $\epsilon_1\theta(t_c) = 1$ and its location is at

$$\lambda_1 = \tfrac{1}{2} + k, \quad (k = 0, \pm1, \ldots). \qquad (15)$$

Note that each singularity then appears along one vortex line. Although $\bar{a}^{(0)}_{n,\pm1}$ and $\bar{c}^{(0)}_{n,\pm1}$ behave like $n^{-3/2}$ at large n, the above mentioned modification is $O(\epsilon_2 t^2) \ll 1$ so that it may be understood that the characteristic of the singularity, i.e. $\bar{a}^{(0)}_{n,0} \propto n^{-5/2}$ at large n, suffers no significant change in three dimensions.

Interpretation (b)

As shown below, the three-dimensional profile (13a–c) is also consistent with the interpretation that it is due to the modification of only the phase λ_1 in the two-dimensional sheet profile. Equation (13a) and (13c) are equivalent to

$$x(\lambda_1,\lambda_2,t) \approx \lambda_1 - \frac{1}{2\pi^2 t}\sum_{n=1}^{\infty}(\epsilon_1\theta)^n \bar{a}_{n,0}^{(0)} \sin 2\pi n\{\lambda_1 + \tfrac{1}{2} - 2\pi^2\alpha(n)\delta\epsilon_2 t^2 \sin 2\pi\delta\lambda_2\}, \tag{16}$$

and

$$z(\lambda_1,\lambda_2,t) \approx -\frac{1}{2\pi^2 t}\sum_{n=1}^{\infty}(\epsilon_1\theta)^n \bar{a}_{n,0}^{(0)} \sin 2\pi n\{\lambda_1 + \tfrac{1}{2} - 2\pi^2\beta(n)\delta\epsilon_2 t^2 \sin 2\pi\delta\lambda_2\}, \tag{17}$$

respectively, where $n\alpha(n) \equiv \bar{a}_{n,1}^{(0)}/\bar{a}_{n,0}^{(0)}$, $n\beta(n) \equiv \bar{c}_{n,1}^{(0)}/\bar{a}_{n,0}^{(0)}$, and we have neglected a term associated with $\bar{c}_{0,1}^{(0)}$ which is irrelevant to the singularity analysis. Since $\alpha(n) = \beta(n) \sim (2\pi)^{\frac{1}{2}} C_\delta$ for large n, (16) and (17) are compatible with the interpretation that the singularity of the same form as in two-dimensional motion appears at t_c and it is distributed along the curves given by

$$\lambda_1 = k + \tfrac{1}{2} + 2\pi^2\alpha(n)\delta\epsilon_2 t^2 \sin\delta\lambda_2, \tag{18}$$

where $k = 0, \pm1, \pm2, \cdots$. In contrast to *Interpretation* (a), these singularity curves are then different from vortex lines satisfying $\lambda_1 =$ constant (these cannot occur in two dimensions).

Interpretation (c)

The assumption that the three-dimensional correction come from the modification of only θ in two-dimensional profile also leads to the $n^{-3/2}$ behavior of $\mathbf{A}_{n,\pm1}$. If this is the case, then the singularity time depends on the spanwise coordinate λ_2. However this possibility can be excluded at the leading-order approximation for the present problem because this assumption is incompatible with $\bar{a}_{n,1}^{(0)} = \bar{a}_{n,-1}^{(0)}$ and $\bar{c}_{n,1}^{(0)} = \bar{c}_{n,-1}^{(0)}$ as shown in (13a) and (13c).

The analytical results in IK do not rule out possibilities other than interpretations (a) and (b), and insufficient for the full characterization of the singularity in three dimensions. In order to get further understanding of the singularity formation, we study the problem by numerical simulation in the following.

3 Numerical method

Our numerical method is on the basis of the Lagrangian representation of the three-dimensional motion of a vortex sheet. For simplicity, we set the aspect ratio δ to be unity hereafter. Since the sheet at time $t \geq 0$ satisfies

$$\mathbf{R}(\lambda_1+n,\lambda_2+m,t) = \mathbf{R}(\lambda_1,\lambda_2,t) + n\begin{pmatrix}1\\0\\0\end{pmatrix} + m\begin{pmatrix}0\\1\\0\end{pmatrix}, \tag{19}$$

the domain of integration in (3) can be reduced to a fundamental periodic domain in (λ_1,λ_2)-space by introducing a double periodic Green's function:

$$\hat{G} = \frac{1}{4\pi}\sum_n\sum_m \frac{1}{\{(x-x'-n)^2+(y-y'-m)^2+(z-z')\}^{1/2}}, \tag{20}$$

where we have put $\mathbf{R} = (x,y,z)$ and $\mathbf{R}' = (x',y',z')$ by assuming $0 \leq \lambda_1, \lambda_2, \lambda_1', \lambda_2' < 1$. We apply the Ewalt sum technique (cf. Baker et al. [1]) for the evaluation of $\hat{G}$. The fundamental domain

is described by $N \times M$ mesh points distributed uniformly in the (λ_1, λ_2)-space such as $\mathbf{R}_{I,J} \equiv \mathbf{R}(I\Delta\lambda_1, J\Delta\lambda_2, t)$ where $\Delta\lambda_1 = 1/N$, $\Delta\lambda_2 = 1/M$, $I = 0, 1, \cdots, N-1$ and $J = 0, 1, \ldots, M-1$. The fast Fourier transforms are used to evaluate $\partial\mathbf{R}/\partial\lambda_2$ at the mesh points with high accuracy. The integration with respect to λ_1 and λ_2 is approximated by trapezoidal quadrature with omitting the singular contribution at $(\lambda_1, \lambda_2) = (\lambda_1', \lambda_2')$.

A system of $3 \times N \times M$ ordinary differential equations thus obtained were solved numerically by the 4th order Runge-Kutta method by using the time step $\Delta t = 0.01$. As introduced by Krasny [5], we used a Fourier filter to control the errors induced by round-off error; Fourier coefficients $\mathbf{A}_{n,m}$ which are less than 10^{-L} were set to zero at the end of every time step. We set the filter level at $L = 13$ in the calculation performed in 16 decimal digits arithmetic. Parameters used in the Ewalt sum were set so as to make the error in the approximation for the double-periodic Green's function to be less than 10^{-8}. For simplicity, we set $\epsilon_1 = \epsilon_2 (\equiv \epsilon)$ in (2), and studied the following two cases: $\epsilon = 0.001$ and 0.01. For $\epsilon = 0.001$, we set $(N, M) = (60, 30)$, $(90, 30)$ or $(120, 30)$, and for $\epsilon = 0.01$, $(N, M) = (60, 30)$ or $(120, 30)$. We used smaller number of mesh points in the spanwise (λ_2) direction than in the streamwise (λ_1) direction because the analytical results in IK suggest that even at the singularity time, the sheet shape is smooth enough in the spanwise direction.

4 Numerical results

4.1 $\epsilon = 0.001$

For $\epsilon = 0.001$ with $(N, M) = (60, 30)$, we integrated the system up to $t = 1.16$. The simulation showed no significant change in the sheet shape up to the time. Figure 1 shows the plot $\ln|\mathbf{A}_{n,m}(t)|$ vs. $\ln n$ with $m = 0, 1, 2, 3$ at $t = 1.10, 1.12$ and 1.14. At the early stage of evolution the spectrum falls off sufficiently rapidly with n (figure omitted), but at the later time the high wave number (large n) mode gets larger and larger and the spectrum attain the form plotted in the figure. It is seen in the figure that the curves of $\ln|\mathbf{A}_{n,m}(t)|$ vs. $\ln n$ $(m = 0, 1, 2)$ at $t = 1.10$ look like convex, while those at $t = 1.14$ look like concave, and between $t = 1.10$ and 1.14 they look like straight lines. The slopes of the lines for $(n, 0)$ and $(n, 1)$ modes are quite close to the theoretical values $-5/2$ and $-3/2$, respectively, which are also plotted in the figure. Note that IK predicts that a singularity appears at $t \sim 1.116$ for $\epsilon = 0.001$. This value 1.116 is consistent with the value $1.1 \sim 1.14$ suggested from Fig. 1.

A bird's-eye view of the vorticity density $|\mathbf{\Omega}| \equiv |\partial\mathbf{R}/\partial\lambda_2|/|(\partial\mathbf{R}/\partial\lambda_1) \times (\partial\mathbf{R}/\partial\lambda_2)|$ at $t = 1.14$ as a function of (λ_1, λ_2) is shown in Fig. 2. It is seen that the profile of the vorticity density forms a cusp-like shape at $t = 1.14$. The simulation showed that the profiles of $\partial x/\partial\lambda_1$ and $\partial z/\partial\lambda_1$ as functions of (λ_1, λ_2) also look cusp-like at $t = 1.14$ (figures omitted). The location of singularity may be determined by investigating the peak position of the profile of $|\mathbf{\Omega}|$.

In order to specify the peak position, we first computed an interpolated function $|\mathbf{\Omega}|$ of λ_1 for a fixed $\lambda_2 = J\Delta\lambda_2$ by using cubic spline, and then determined the λ_1-value which gives the maximum of $|\mathbf{\Omega}|$ by using inverse parabolic interpolation. Figure 3 shows the λ_1-value of the peak position of $|\mathbf{\Omega}|$ at $t = 1.12$ as a function of λ_2. The peak positions of $\partial x/\partial\lambda_1$ and $\partial z/\partial\lambda_1$ at $t = 1.10$ are also plotted in the figure. Each of these curves is seen to be quite close to a simple sinusoidal curve. The simulation showed that this is also the case for $0 < t \leq 1.14$.

Figure 4 shows the λ_1-values of the peak positions for fixed J as functions of time t, where we have put $J = 8$, i.e. $\lambda_2 \approx 1/4$, at which the sinusoidal curves deviate most from the center $\lambda_1 = 1/2$ (see Fig. 3). It can be observed that the curves for $|\mathbf{\Omega}|$, $\partial x/\partial\lambda_1$ and $\partial z/\partial\lambda_1$ collapse into a point at $t \approx 1.14$. These results can be explained by Interpretation (b). In Interpretation (b), it is expected that a singularity appear along a simple sinusoidal curve given by (18). For $\epsilon = 0.001$, the curve is

given by

$$\lambda_1 = 0.5 + \gamma \sin(2\pi\lambda_2), \qquad \gamma = -0.0007, \tag{21}$$

where we have used the theoretical values $t_c = 1.116$ and $\alpha(n) \sim -0.0294$ for large n and $\delta = 1$ (the latter was obtained from a plot of $\alpha(n)$ *vs.* $1/n$ by solving numerically (8), (9a) and (9b) with $\delta = 1$). As shown in Fig. 3, the curves look sinusoidal in agreement with (8), and the numerical estimate from Fig. 4 gives $\gamma \approx -0.0003$ at $t = 1.14$, which is in fair quantitative agreement with (8).

For $\epsilon = 0.001$ with $(N, M) = (120, 30)$, we integrated the system up to $t = 1.04$. The simulation showed no significant change in the sheet profile before $t = 1.00$, but the motion of the 120×30 points became irregular at $t \approx 1.04$. Figure 5 shows a bird's-eye view of the vorticity density $|\mathbf{\Omega}|$ at $t = 0.99$ as a function of (λ_1, λ_2). Differently from the case of $(N, M) = (60, 30)$, it is seen that there are two peaks (not one) in one fundamental periodic domain of the profile. Two peaks were also observed in the profiles of the functions $\partial x/\partial\lambda_1$ and $\partial z/\partial\lambda_1$ of (λ_1, λ_2) at $t = 0.99$, as well as in the profiles of $|\mathbf{\Omega}|$, $\partial x/\partial\lambda_1$ and $\partial z/\partial\lambda_1$ in the case of $(N, M) = (90, 30)$ at $t \approx 1.06$ (figures omitted).

The spectrum $\ln|\mathbf{A}_{n,m}(t)|$ vs. $\ln n$ with $m = 0, 1, 2, 3$ at $t = 0.96, 0.97, 0.98$ and 0.99 is shown in Fig. 6a. It may be understood that the wavy nature of the spectrum reflects the existence of the two peaks, i.e. two singularities. Noting that the spacings, say Δn, between the minima of the wavy curves are the same, i.e. $\Delta n \approx 14$, we assume the following expression for the sheet profile (on the basis of Interpretation (b)):

$$\begin{aligned} x(\lambda_1, \lambda_2, t) &\approx \lambda_1 - \frac{1}{2\pi^2 t} \sum_{n=1}^{\infty} (\epsilon_1\theta)^n \bar{a}^{(0)}_{n,0} \Big\{ \sin 2\pi n \Big[\lambda_1 + \tfrac{1}{2} - \tfrac{1}{2}d - 2\pi^2\alpha(n)\delta\epsilon_2 t^2 \sin 2\pi\delta\lambda_2\Big] \\ &\qquad + \sin 2\pi n \Big[\lambda_1 + \tfrac{1}{2} + \tfrac{1}{2}d - 2\pi^2\alpha(n)\delta\epsilon_2 t^2 \sin 2\pi\delta\lambda_2\Big] \Big\} \\ &\approx \lambda_1 - \frac{1}{\pi^2 t} \sum_{n=1}^{\infty} (\epsilon_1\theta)^n \bar{a}^{(0)}_{n,0} \cos(\pi n d) \sin 2\pi n \Big[\lambda_1 + \tfrac{1}{2} - 2\pi^2\alpha(n)\delta\epsilon_2 t^2 \sin 2\pi\delta\lambda_2\Big], \end{aligned} \tag{22}$$

where d is the difference in the λ_1-coordinate of two peaks. The above mentioned spacing, i.e. $\Delta n \approx 14$, corresponds to $d \approx 1/14$. With (22) in mind, we plot $\ln|\mathbf{A}_{n,m}(t)| - \ln|\cos(\pi n d)|$ vs. $\ln n$ in Fig. 6b. The curves in Fig. 6b look similar to those in Fig. 1 and have slopes close to the theoretical values $-5/2$ and $-3/2$ for $m = 0$ and $m = 1$, respectively, at $t \approx 0.99$.

As in the case of $(N, M) = (60, 30)$, the λ_1-values of the peak positions of $|\mathbf{\Omega}|$ are plotted in Figs. 7 (*a*) and (*b*) as functions of λ_2 at $t = 0.98, 0.99$ and 1.00. Each of the curves in Figs. 7a,b at the same time corresponds to one of the two peaks in the profile of $|\mathbf{\Omega}|$ at that time. Similar curves for $\partial x/\partial\lambda_1$ and $\partial z/\partial\lambda_1$ are also plotted in Figs. 7a,b. It can be observed in each figure that the curves look like simple sinusoidal and at a certain time ($t \approx 1.00$), the three curves corresponding to $|\mathbf{\Omega}|$, $\partial x/\partial\lambda_1$ and $\partial z/\partial\lambda_1$ collapse into one curve. These properties are similar to those in the case of $(N, M) = (60, 30)$ except for the difference in the number of peaks; one peak in $(N, M) = (60, 30)$, while two peaks in $(N, M) = (120, 30)$.

4.2 $\epsilon = 0.01$

For $\epsilon = 0.01$ with $(N, M) = (120, 30)$, we integrated the system up to $t = 0.50$, at which sharp peaks appear in the profile of the functions $|\mathbf{\Omega}|$, $\partial x/\partial\lambda_1$ and $\partial z/\partial\lambda_1$ of (λ_1, λ_2). Figure 8 shows $\ln|\mathbf{A}_{n,m}(t)|$ vs. $\ln n$ with $m = 0, 1, 2, 3$ at $t = 0.50$. The spectrum has a complicated form reflecting the stronger nonlinearity of the system.

In order to see the λ_2-dependence, we plot $|\mathbf{\Omega}(\lambda_1, \lambda_2 = 0)|$ and $|\mathbf{\Omega}(\lambda_1, \lambda_2 = 1/4)|$ in Fig. 9. It can be seen that the two lines are clearly different. In order to characterize this difference quantitatively, let us define $\zeta(\lambda_1, \lambda_2) = x(\lambda_1, \lambda_2) + \mathrm{i}z(\lambda_1, \lambda_2)$ and the spectra $A_n^{[0]}$ and $A_n^{[1/4]}$ by the following relations:

$$\begin{aligned} \zeta(\lambda_1, 0) &= \lambda_1 + \sum_n A_n^{[0]} \exp\{2\pi \mathrm{i} n \lambda_1\}, \\ \zeta(\lambda_1, \tfrac{1}{4}) &= \lambda_1 + \sum_n A_n^{[1/4]} \exp\{2\pi \mathrm{i} n \lambda_1\}. \end{aligned}$$

Figure 10a shows $\ln|A_n^{[0]}|$ and $\ln|A_n^{[1/4]}|$ vs. $\ln n$ at $t = 0.50$. Although the two curves seem to be quite similar to each other, a close inspection shows that there exists a systematic difference between them. Figure 10b shows $\ln|A_n^{[1/4]}| - \ln|A_n^{[0]}|$ vs. $\ln n$ at $t = 0.50$. If we assume the forms $A_n^{[0]} \propto n^{-p}$ and $A_n^{[1/4]} \propto n^{-q}$, $\ln|A_n^{[1/4]}| - \ln|A_n^{[0]}| = (p - q)\ln n$; figure 10b suggests $p - q \approx 0.045$, i.e. the sheet profile is more singular at $\lambda_2 = \frac{1}{4}$ than at $\lambda_2 = 0$.

5 Conclusions and discussion

We have simulated the three-dimensional motion of vortex sheet on the basis of a Lagrangian representation of the motion.

For $\epsilon = 0.001$ with $(N, M) = (60, 30)$, the numerical results confirm the previous analytical results, i.e. $\mathbf{A}_{n,0} \propto n^{-5/2}$ and $\mathbf{A}_{n,\pm 1} \propto n^{-3/2}$ at large n, in IK. The profiles of the functions $|\mathbf{\Omega}|$, $\partial x/\partial\lambda_1$ and $\partial z/\partial\lambda_1$ of (λ_1, λ_2) exhibit cusp-like shapes at $t \approx 1.14$, and at that time the λ_1-value of the peak positions of these profiles shows almost the same sinusoidal dependence on λ_2. These results suggest that a singularity appears along a simple curve depending sinusoidally on λ_2. These can be explained by Interpretation (b). Note that the curve does not coincide with one vortex line satisfying λ_1 =constant (such discrepancy cannot occur in two dimensions).

For $\epsilon = 0.001$ with $(N, M) = (120, 30)$, the profiles of the functions $|\mathbf{\Omega}|$, $\partial x/\partial\lambda_1$ and $\partial z/\partial\lambda_1$ of (λ_1, λ_2) exhibit two peaks per one fundamental periodic domain at $t = 0.99$; the result of the computation with $(N, M) = (90, 30)$ also exhibited two peaks in those profiles. The difference in the number of peaks might be understood as due to the lack of resolution of the system with $(N, M) = (60, 30)$ to detect two peaks resolved by $(N, M) = (90, 30)$ and $(120, 30)$. In this context, it may be worthwhile to mention our recent preliminary simulations based on point vortex approximation (cf. Krasny [5]) for the two-dimensional problem ($\epsilon_2 = 0$ in (2)); they have also shown the similar, i.e. for $\epsilon_1 = 0.002$, a single peak appears with $N = 60$ and 90, while double peaks with $N = 120$ and 240. The two-dimensional simulations have also shown that for $\epsilon_1 = 0.001$ a single peak appears with $N = 240$. If this property exists also in three dimensions, it is expected that for the smaller initial amplitude of disturbance than $\epsilon = 0.001$, a single peak (singularity) would appear even in the higher resolution computation such as $(N, M) = (90, 30)$ and $(120, 30)$. It may be then concluded that the initial amplitude $\epsilon = 0.001$ is not sufficiently small for the behavior to be explained by IK. It was found that the peaks of the functions $|\mathbf{\Omega}|$, $\partial x/\partial\lambda_1$ and $\partial z/\partial\lambda_1$ of (λ_1, λ_2) have simple sinusoidal dependence on λ_2 in spite of the difference of the number of the peaks according to the resolution of the system. This nature can be explained by Interpretation (b) with the assumption in (22).

The computation for the stronger nonlinear case, $\epsilon = 0.01$ with $(N, M) = (120, 30)$, showed the stronger λ_2-dependence of the singularity. For example, the characteristic exponent of the singularity defined in the previous section was found to depend on λ_2 remarkably. (The simulation for $\epsilon = 0.001$ with $(N, M) = (120, 30)$ shows a small dependence on λ_2; $p - q \approx 0.0007$.) Presumably

the strong nonlinear nature as observed in the computation for $\epsilon = 0.01$ with $(N, M) = (120, 30)$ is beyond the the approximation in IK.

The resolution of the present computations are clearly insufficient for the full characterization of the singularity, and the results presented in this paper are only suggestive. It would be interesting to perform computations with higher resolution for the characterization.

References

[1] Baker, G.R., Meiron, D.I. and Orszag, S.A., "Boundary Integral Methods for Axisymmetric and Three-Dimensional Rayleigh-Taylor Instability Problems," *Physica D*, **12**, pp. 19–31, 1984.

[2] Caflisch, R.E., "Mathematical Analysis of Vortex Dynamics," Proc. Workshop on Mathematical Aspects of Vortex Dynamics, edited by R.E. Caflisch, pp. 1–24. SIAM, 1989.

[3] Ishihara, T. and Kaneda, Y., 'Singularity Formation in Three-Dimensional Motion of a Vortex Sheet," *J. Fluid Mech.*, **300**, pp. 339–366, 1995.

[4] Kaneda, Y., "A Representation of the Motion of a Vortex Sheet in a Three-Dimensional Flow," *Phys. Fluids A*, **2**, pp. 458–461, 1990. (Also presented at the meeting held in July, 1989 at the Research Institute of Mathematical Science, Kyoto University.)

[5] Krasny, R., "A Study of Singularity Formation in a Vortex Sheet by the Point-Vortex Approximation," *J. Fluid Mech.*, **167**, pp. 65–93, 1986.

[6] Moore, D.W., "The Spontaneous Appearance of a Singularity in the Shape of an Evolving Vortex Sheet," *Proc. R. Soc. Lond. A*, **134**, pp. 170–191, 1979.

[7] Meiron, D.I., Baker, G.R. and Orszag, S.A., "Analytical Structure of Vortex Sheet Dynamics. Part 1. Kelvin-Helmholtz Instability," *J. Fluid Mech.*, **114**, pp. 283–298, 1982.

[8] Shelley, M., "A Study of Singularity Formation in Vortex-Sheet Motion by a Spectrally Accurate Vortex Method," *J. Fluid Mech.*, **244**, pp. 493–526, 1992.

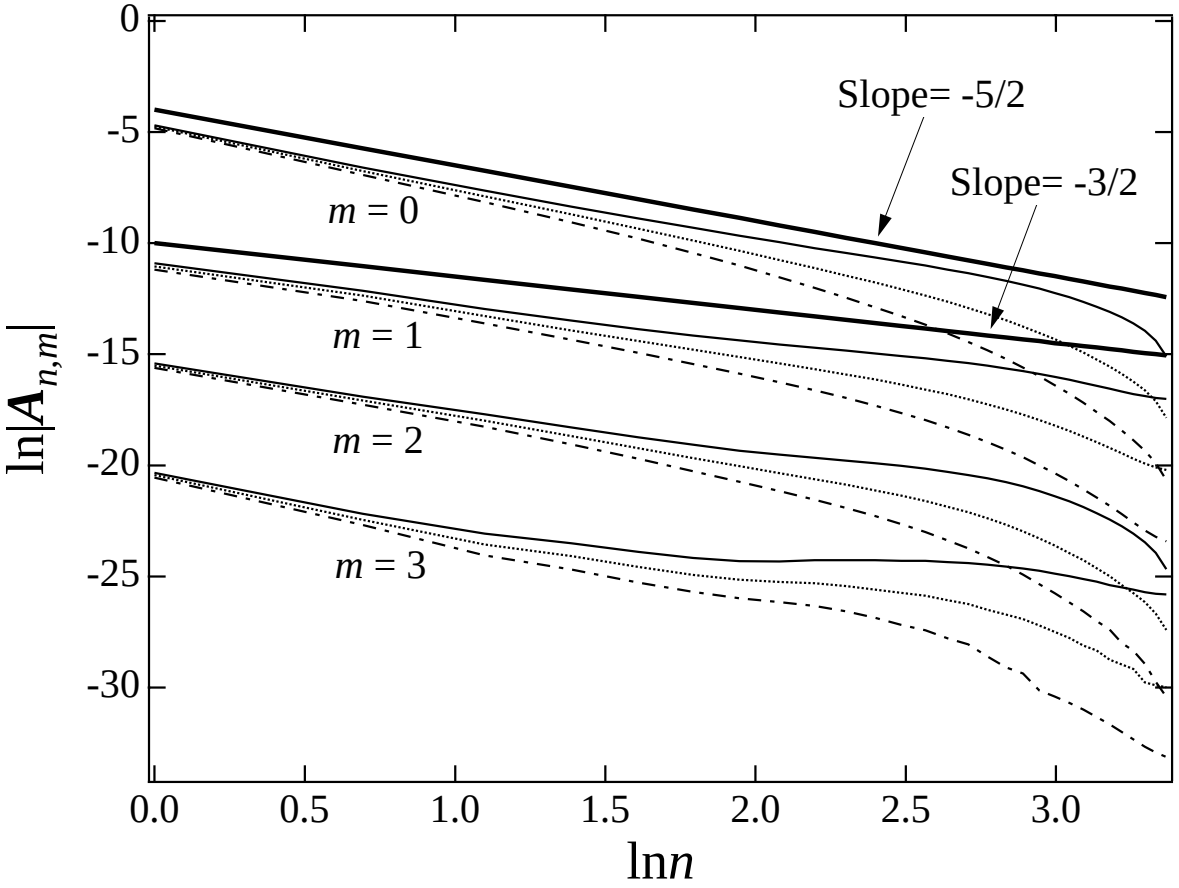

Figure 1: $\ln|\mathbf{A}_{n,m}(t)|$ vs. $\ln n$ with $m = 0, 1, 2, 3$ at $t = 1.10$ (dot-dash-lines), 1.12 (dotted lines) and 1.14 (solid lines) by the numerical solution for $\epsilon = 0.001$ with $(N, M) = (60, 30)$. The thick solid lines have the indicated slopes.

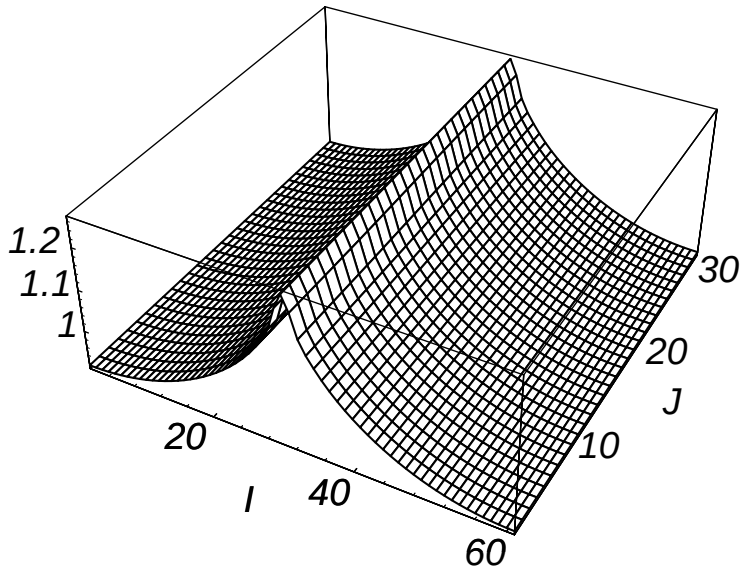

Figure 2: A bird's-eye view of the vorticity density $|\mathbf{\Omega}|$ as a function of (λ_1, λ_2) at $t = 1.14$ by the numerical solution for $\epsilon = 0.001$ with $(N, M) = (60, 30)$. The mesh point (I, J) in the figure corresponds to $(\lambda_1, \lambda_2) = (I/N, J/M)$.

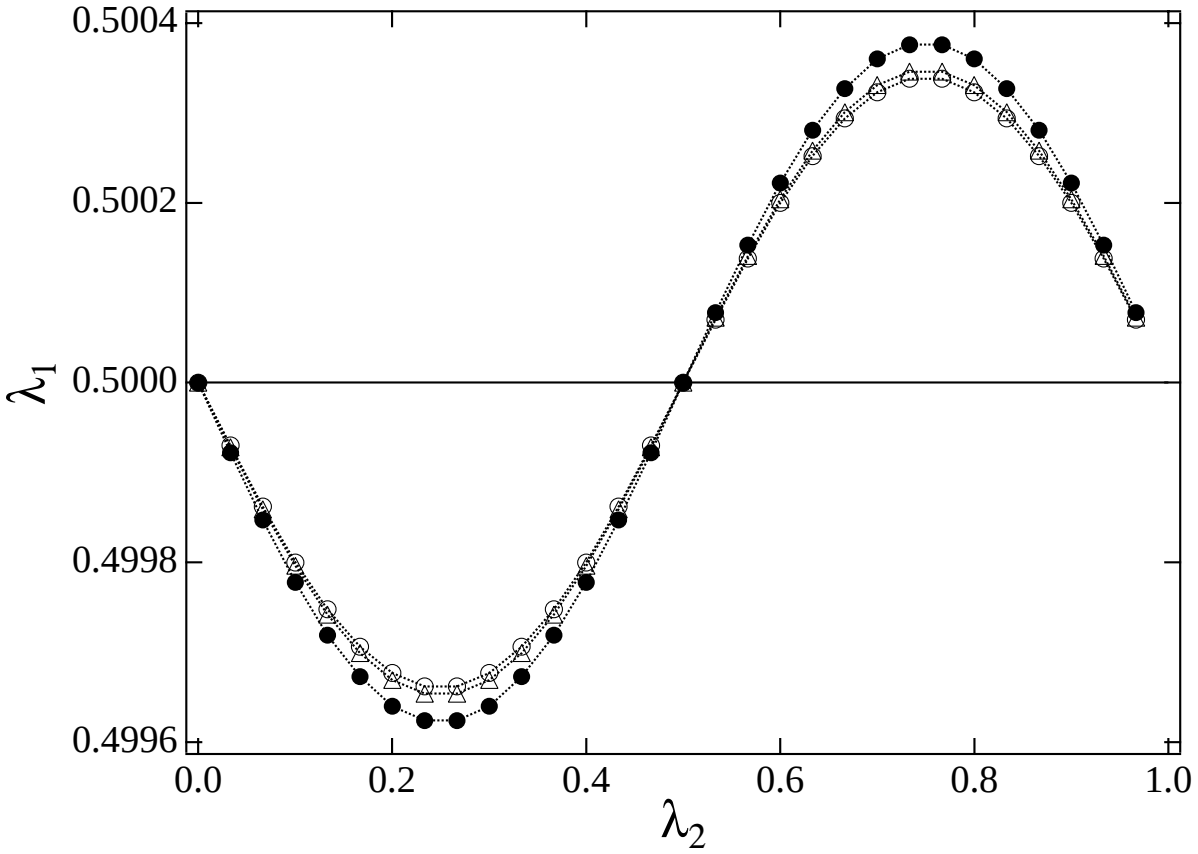

Figure 3: The λ_1-values of the peak positions of $|\mathbf{\Omega}|$ ($\circ$), $\partial x/\partial\lambda_1$ ($\triangle$) and $\partial z/\partial\lambda_1$ ($\bullet$) as functions of λ_2 at $t = 1.12$ by the numerical solution for $\epsilon = 0.001$ with $(N, M) = (60, 30)$.

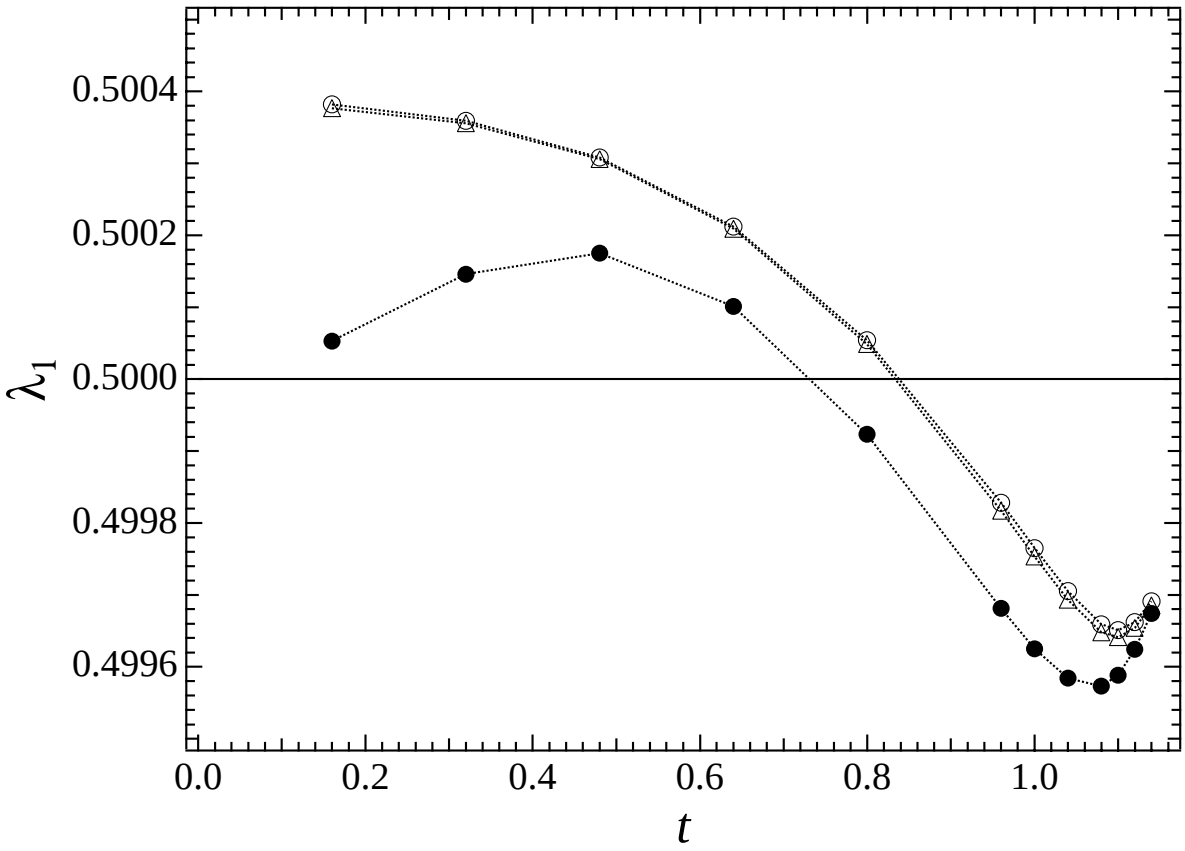

Figure 4: The λ_1-values of the peak positions of $|\mathbf{\Omega}|$ ($\circ$), $\partial x/\partial\lambda_1$ ($\triangle$) and $\partial z/\partial\lambda_1$ ($\bullet$) for $J = 8$ ($\lambda_2 \approx 1/4$) as functions of time t by the numerical solutions for $\epsilon_1 = 0.001$ with $(N, M) = (60, 30)$.

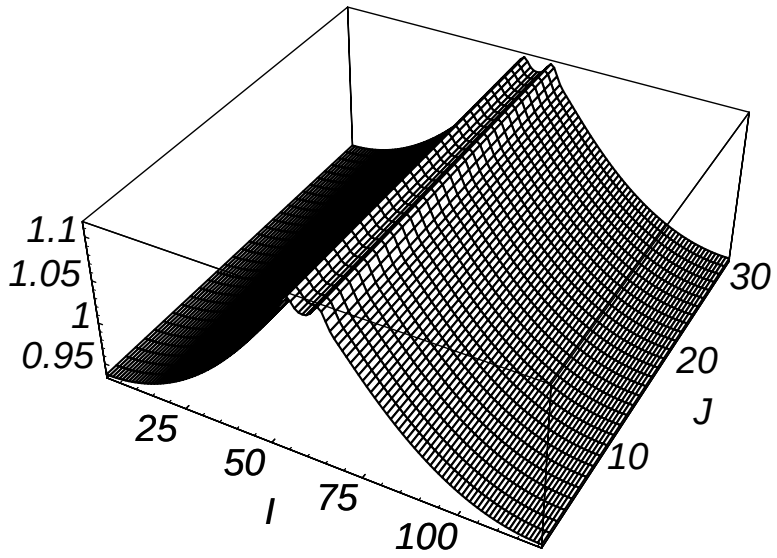

Figure 5: A bird's-eye view of the vorticity density $|\mathbf{\Omega}|$ as a function of (λ_1, λ_2) at $t = 0.99$ by the numerical solution for $\epsilon = 0.001$ with $(N, M) = (120, 30)$. The mesh point (I, J) in the figure corresponds to $(\lambda_1, \lambda_2) = (I/N, J/M)$.

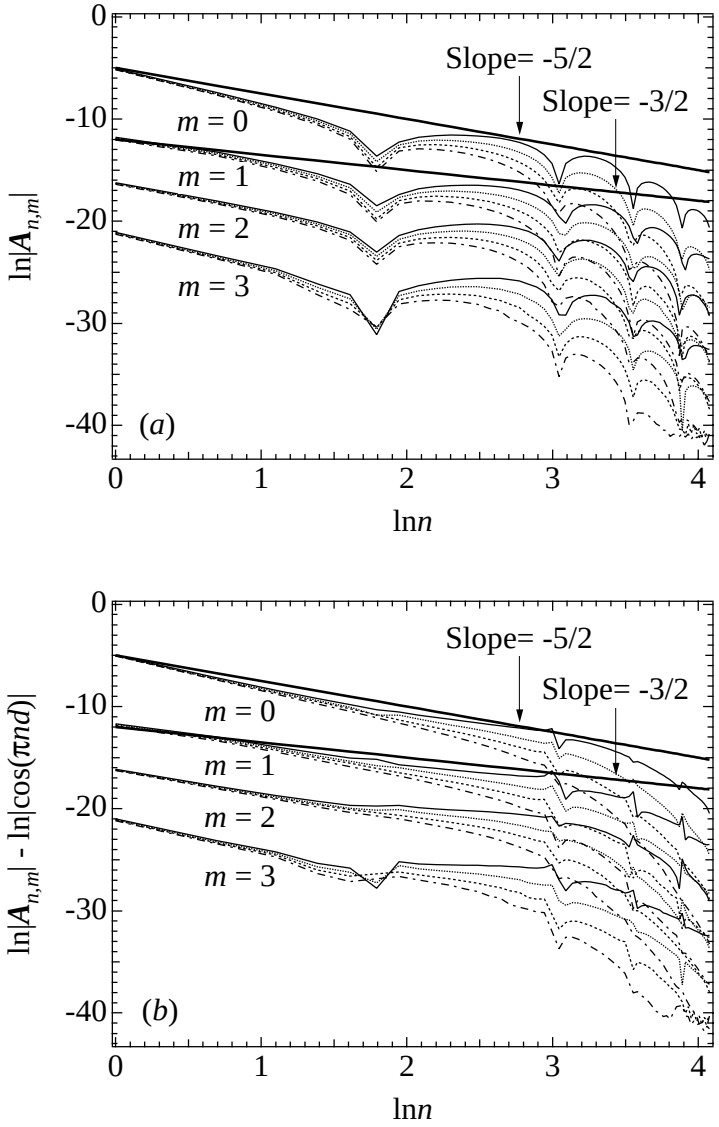

Figure 6: (a) $\ln|\mathbf{A}_{n,m}(t)|$ vs. $\ln n$ with $m = 0, 1, 2, 3$ at $t = 0.96$ (dot-dash-lines), 0.97 (dashed lines), 0.98 (dotted lines) and 0.99 (solid lines) by the numerical solutions for $\epsilon = 0.001$ with $(N, M) = (120, 30)$. The thick solid lines have the indicated slopes. (b) The values of $\ln|\mathbf{A}_{n,m}(t)|$ in (a) are replaced by $\ln|\mathbf{A}_{n,m}(t)| - \ln|\cos(\pi n d)|$ with $d = 1/14$ which corresponds to the spacings $\Delta n \approx 14$ between the minima of the wavy curves in (a).

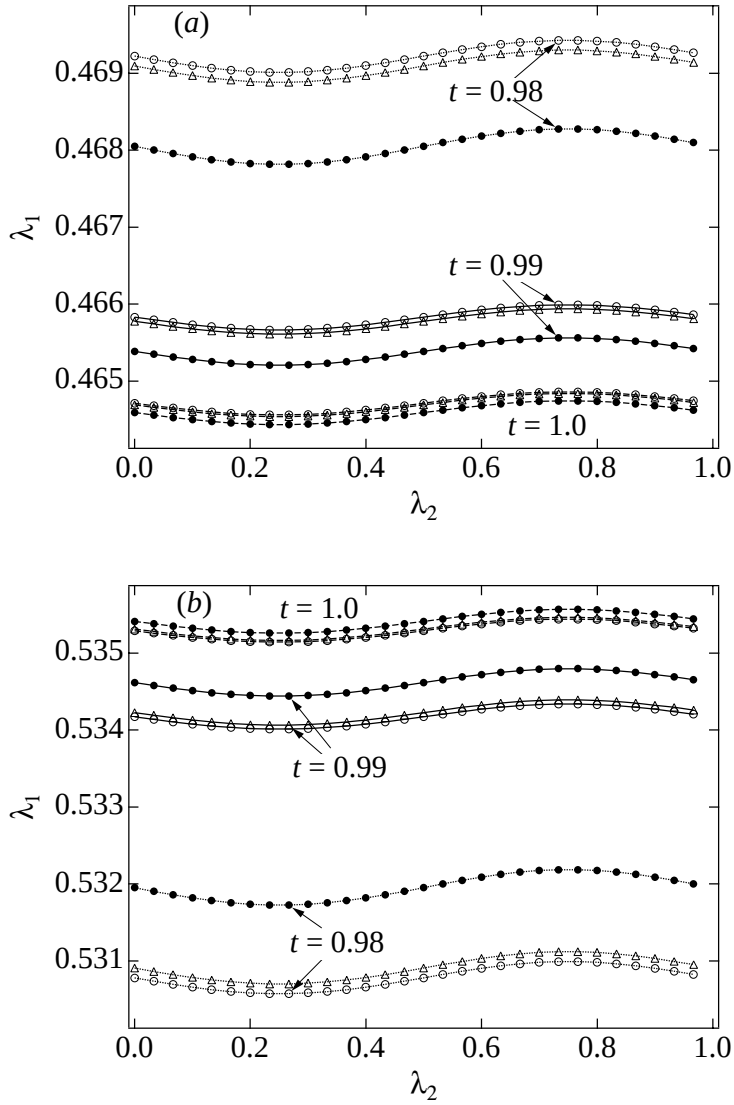

Figure 7: The λ_1-values of the peak positions of $|\mathbf{\Omega}|$ ($\circ$), $\partial x/\partial\lambda_1$ ($\triangle$) and $\partial z/\partial\lambda_1$ ($\bullet$) as functions of λ_2 at $t = 0.98$, 0.99 and 1.0. Each of the curves in Figs. 7a,b at the same time corresponds to one of the two peaks in the profiles of $|\mathbf{\Omega}|$, $\partial x/\partial\lambda_1$ and $\partial z/\partial\lambda_1$ at that time.

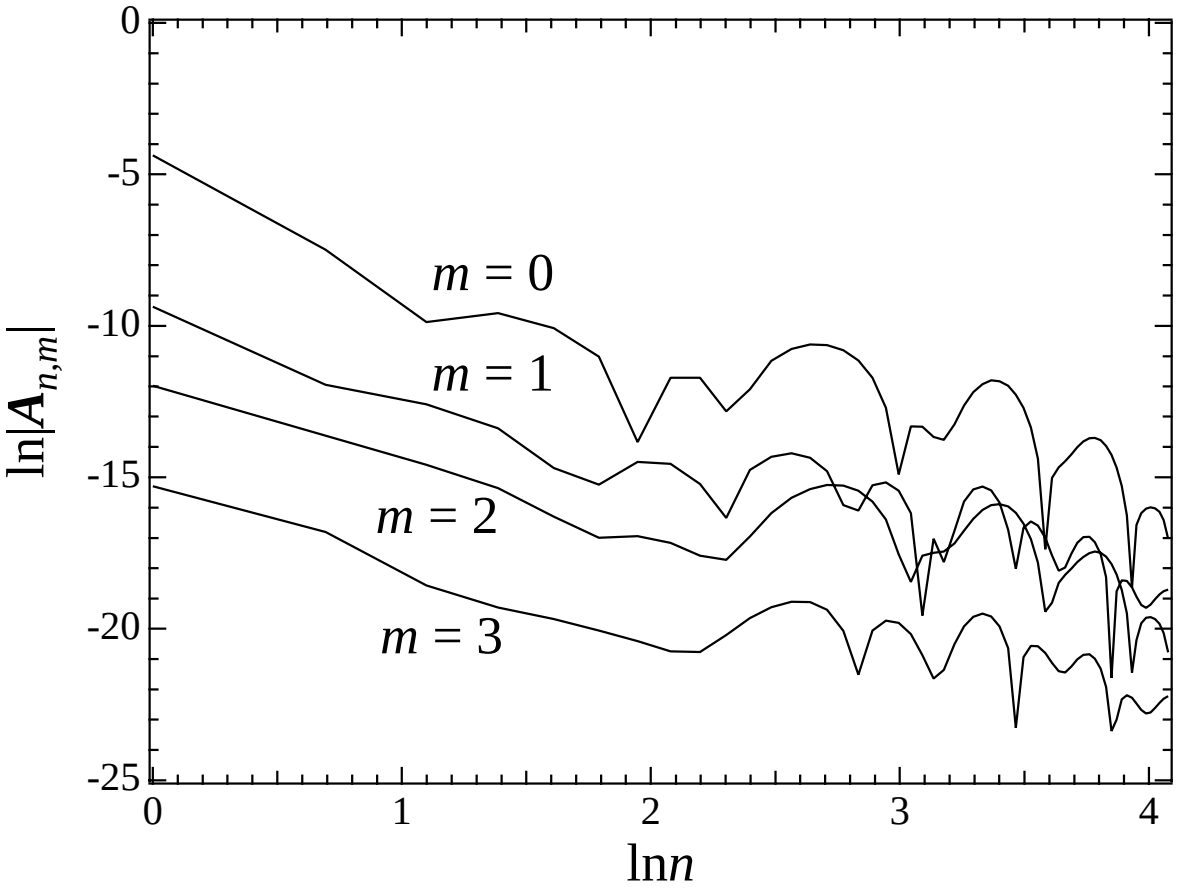

Figure 8: $\ln|\mathbf{A}_{n,m}(t)|$ vs. $\ln n$ with $m = 0, 1, 2, 3$ at $t = 0.50$ by the numerical solutions for $\epsilon = 0.01$ with $(N, M) = (120, 30)$.

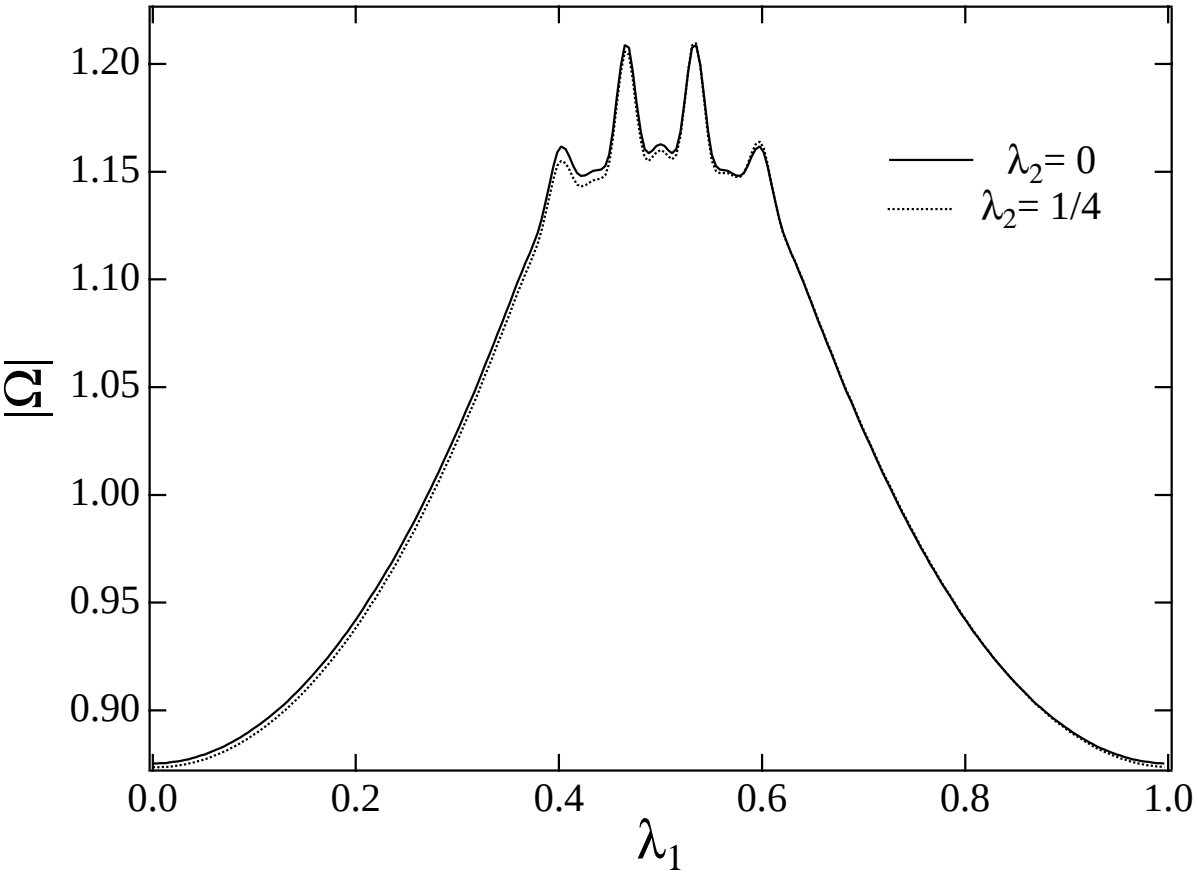

Figure 9: The profiles of $|\mathbf{\Omega}|$ at $\lambda_2 = 0$ and $1/4$ at $t = 0.50$ by the numerical solution for $\epsilon = 0.01$ with $(N, M) = (120, 30)$.

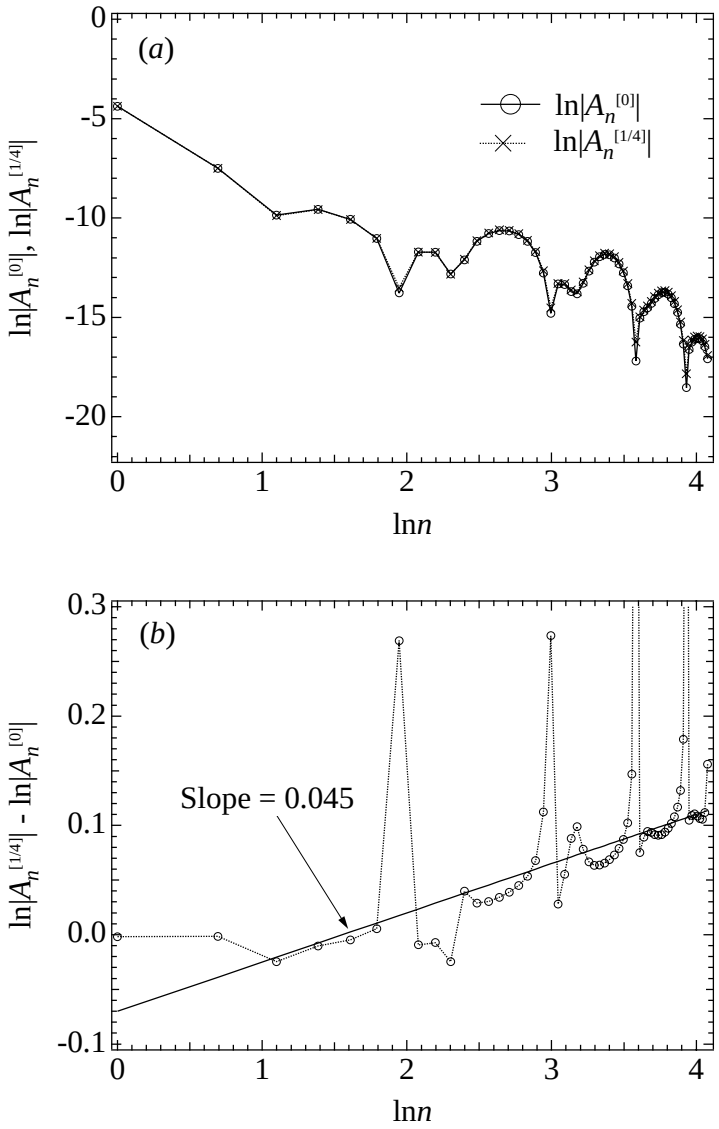

Figure 10: (a) $\ln|A_n^{[0]}|$ and $\ln|A_n^{[1/4]}|$ vs. $\ln n$ at $t = 0.50$ by the numerical solution for $\epsilon = 0.01$ with $(N, M) = (120, 30)$. (b) $\ln|A_n^{[0]}| - \ln|A_n^{[1/4]}|$ vs. $\ln n$ at $t = 0.50$. The solid line has the indicated slope.